RESEARCH ARTICLE

Synergy of MXene with Se Infiltrated Porous N-Doped Carbon Nanofibers as Janus Electrodes for High-Performance Sodium/Lithium–Selenium Batteries

Jiayi Li, Jianjun Song, Linqu Luo, Hongwei Zhang, Junan Feng, Xiaoxian Zhao, Xin Guo, Hanghang Dong, Shuangqiang Chen, Hao Liu, Guangjie Shao, Thomas. D. Anthopoulos, Yaqiong Su,* Fengyun Wang,* and Guoxiu Wang**

Metal–selenium (M–Se) batteries are considered promising candidates for next-generation battery technologies owing to their high energy density and high-rate capability. However, Se cathode suffers from poor cycling performance and low Coulombic efficiency, owing to the shuttle effect of polyselenides. Herein, it is reported the incorporation of $Ti_3C_2T_x$ MXene onto Se infiltrated porous N-doped carbon nanofibers (PNCNFs) to construct free-standing Janus PNCNFs/Se@MXene cathodes for high-performance Na–Se and Li–Se batteries. The increase of pyrrolic-N content and the porous structure of the PNCNFs is conducive to enhancing the adsorption of Na_2Se and alleviating the shuttle effect. Meanwhile, density functional theory (DFT) calculations have proven that 2D $Ti_3C_2T_x$ MXene with polar interfaces enables the effective chemical immobilization and physical blocking of polyselenides to suppress the shuttle effect. The unique architecture with $Ti_3C_2T_x$ MXene built on top of interlinked nanofiber ensures the continuous electron transfer for redox reaction. As a result, the novel Janus PNCNFs/Se@MXene electrodes deliver robust rate capabilities and superior long-term cycling stability in both Na–Se and Li–Se batteries. The incorporation of 2D MXene to construct Janus electrodes provides a competitive advantage for selenium-based cathode materials and highlights a new strategy for developing high-performance batteries.

1. Introduction

Renewable energy storage devices with high energy density, excellent cyclic stability, and long cycle life are in great demand for use in portable electronics, electric vehicles, and grid energy storage.[1,2] Among the various new rechargeable battery technologies, room-temperature metal–selenium (e.g., Li–Se and Na–Se) batteries have attracted considerable attention owing to their high theoretical specific capacity (678 mA h g^{-1}), and superior volumetric capacity (3253 mA h cm^{-3}).[3,4] The relatively good electronic conductivity of Se (1×10^{-3} S m^{-1}) also boosts the reaction kinetics with sodium metal which helps improve the overall stability of the system. Moreover, Na is an earth-abundant element, and it undergoes electrochemical reactions similar to Li. These combined advantages make metal–Se batteries technology an attractive choice for large-scale,

J. Li, J. Song, H. Zhang, J. Feng, F. Wang
College of Physics
Qingdao University
Qingdao 266071, P. R. China
E-mail: jianjun.song@qdu.edu.cn; fywang@qdu.edu.cn

L. Luo, Thomas. D. Anthopoulos
Physical Science and Engineering Division
King Abdullah University of Science and
Technology (KAUST)
KAUST Solar Centre
Thuwal 23955-6900, Saudi Arabia

X. Zhao
Department of Chemistry
College of Science
Hebei Agricultural University
Baoding 071001, P. R. China

X. Guo, H. Liu, G. Wang
Centre for Clean Energy Technology
School of Mathematical and Physical Sciences
Faculty of Science
University of Technology Sydney
Broadway, Sydney, NSW 2007, Australia
E-mail: guoxiu.wang@uts.edu.au

H. Dong, S. Chen
Department of Chemical Engineering
School of Environmental and Chemical Engineering
Shanghai University
Shanghai 200444, P. R. China

G. Shao
State Key Laboratory of Metastable Materials
Science and Technology
Yanshan University
Qinhuangdao 066004, P. R. China

higher power densities applications.[5,6] Despite the tremendous potential, the Se cathode suffers from the severe shuttle effect of polyselenide intermediates, which tend to shuttle across the separator and then react with the Na/Li anode during cell operation, ultimately leading to the low utilization rate of active selenium, dramatic capacity fading, and low Columbic efficiency (CE).[3,7,8]

Many efforts have been devoted to alleviating the shuttle effect and improving the cycling stability of metal–Se batteries. The most widely adopted and effective attempt is to incorporate Se with tailor-made conductive carbonaceous hosts, including encapsulation/hybridization of Se with microporous/mesoporous carbon nanofibers,[9–11] carbon nanospheres,[7,12,13] and carbon nanosheets.[1,14,15] These carbon matrixes offer a large pore volume for Se loading and improve the overall electronic conductivity of the electrode.[16,17] Furthermore, heteroatoms doped into carbon matrixes have proved to be an elegant approach to restrain the shuttle effect of polyselenides, and provide more interconnected conductive pathways for fast ionic and electronic transport.[15] For example, Wang's group synthesized N and S dual-doped porous carbon/Se composite coated with polyaniline for Na–Se batteries and exhibited a reversible capacity of 617 mA h g^{-1} after 200 cycles at 0.2 C.[18] Li et al. also reported that N and O dual-doping could boost the interaction between carbon host and Na selenide, and trap polyselenides intermediates, thus preventing the side reaction during cycling.[19]

Recently, MXenes ($M_{n+1}X_nT_x$, where M represents transition metal, X stands for carbon/nitrogen, $n = 1$–4, T_x is surface terminations, such as −O, −OH, and/or −F), as an emerging family of 2D layered materials, which have been reported. They possess extraordinary electronic conductivity, flexibility, hydrophilicity, and compositional diversity. These advantages boost MXenes desirability not only as electrode materials but also as other components in new energy storage devices.[20–23] Particularly, several studies showed that MXenes can effectively restrict the shuttle effect of polysulfides in lithium–sulfur (Li–S) batteries through the strong Ti–S interaction.[24–27] To this end, Zhang et al. reported that polypropylene (PP) separator modified with cetrimonium bromide/carbon nanotube/MXene composite could immobilize polyselenides through the Lewis acid-base interactions between cetrimonium bromide/MXene and polyselenides.[28] Therefore, it will be highly interesting to explore the incorporation of MXene in Se cathodes to overcome the shortcomings of metal–Se batteries.

Herein, we designed and developed a novel flexible Janus PNCNFs/Se@MXene architecture consisting of 1D Se infiltrated porous N-doped carbon nanofibers (PNCNFs/Se) side and 2D Ti$_3$C$_2$T$_x$ MXene side, which was applied as the freestanding cathodes to improve the overall electrochemical

performance of Na–Se and Li–Se batteries. In this unique architecture, PNCNFs with a large surface area are conducive to accommodating Se volume change during cycling and increasing the contact area of the electrode/electrolyte. N-doping creates defects in nanofibers, which provide active sites for Na$^+$ embedding, and a large proportion of pyrrolic-N is more favorable to adsorb Na$_2$Se to improve the utilization rate of Selenium. MXene (Ti$_3$C$_2$T$_x$) can further entrap soluble sodium polyselenides (NaPSe) via the dual physical-chemical blocking effect and in situ anchoring conversion of NaPSe. Moreover, 3D interconnected conductive networks consisting of 1D PNCNFs and 2D MXene sheets facilitate fast electron transfer for redox reactions. Thus, the ensuing devices deliver a reversible specific capacity of 625 mA h g^{-1} after 200 cycles at 0.2 C (1 C = 678 mA g^{-1}) and a high-rate capacity of 411 mA h g^{-1} at 20 C. Importantly, PNCNFs/Se@MXene electrodes show excellent long-term cycling capacity of ≈496 mA h g^{-1} after 500 cycles at 5 C and 348 mA h g^{-1} at 10 C after 5000 cycles. In the case of lithium storage, the novel electrode exhibits a stable capacity (429 mA h g^{-1} at 0.2 C after 200 cycles) and long cycle capacity (303 mA h g^{-1} at 5 C after 3500 cycles) at a high Se loading of ≈74.9 wt%.

2. Results and Discussion

The synthesis strategy for PNCNFs/Se@MXene is schematically illustrated in **Figure 1**a. Polyacrylonitrile (PAN), SiO$_2$ spheres, and *N*, *N*-dimethylformamide (DMF) were uniformly mixed and electrospun into fibrous membranes (Figure 1a; and Figure S1, Supporting Information). The fibrous membranes were stabilized in ambient air, then carbonized at high temperature in Ar. During the carbonization process, SiO$_2$ spheres act as hard templates and PAN is transformed into N-doped carbon nanofibers. Subsequently, the as-prepared nanofibers were immersed in hydrofluoric acid (HF) to remove SiO$_2$ and the initial freestanding and flexible electrode structure is finely maintained. After washing, drying, and infiltrating Se, PNCNFs/Se composites were obtained. Finally, after compounding with Ti$_3$C$_2$T$_x$ MXene laminates (Figure S2, Supporting Information), the as-prepared PNCNFs/Se@MXene electrodes can be directly used as cathodes in Na–Se and Li–Se batteries.

The morphological evolution of SiO$_2$@PAN precursor membrane was monitored by field-emission scanning electron microscopy (FESEM), as shown in Figure S1 (Supporting Information), revealing that SiO$_2$ templating spheres with an average size of about 300 nm are uniformly distributed within NCNFs, promising a uniformity of pore size after removing SiO$_2$. Figure S3 (Supporting Information) displays typical SEM images of carbonized nanofibers before etching which proved that the 1D structure is still maintained with a fiber diameter of ≈700 nm. After etching, the SEM images of porous N-doping carbon nanofibers are presented in Figure 1b; and Figure S4a (Supporting Information), the fiber structure is perfectly maintained with uniformly distributed pores. The porous 1D feature of PNCNFs was further elucidated by transmission electron microscopy (TEM) (Figure 1c; and Figure S4b, Supporting Information). TEM image (Figure 1d) reveals that the average diameter of pores is about 300 nm, which is consistent with

Y. Su
School of Chemistry
Xi'an Key Laboratory of Sustainable Energy Materials Chemistry
MOE Key Laboratory for Nonequilibrium Synthesis and Modulation of Condensed Matter
State Key Laboratory of Electrical Insulation and Power Equipment
Xi'an Jiaotong University
Xi'an 710049, P. R. China
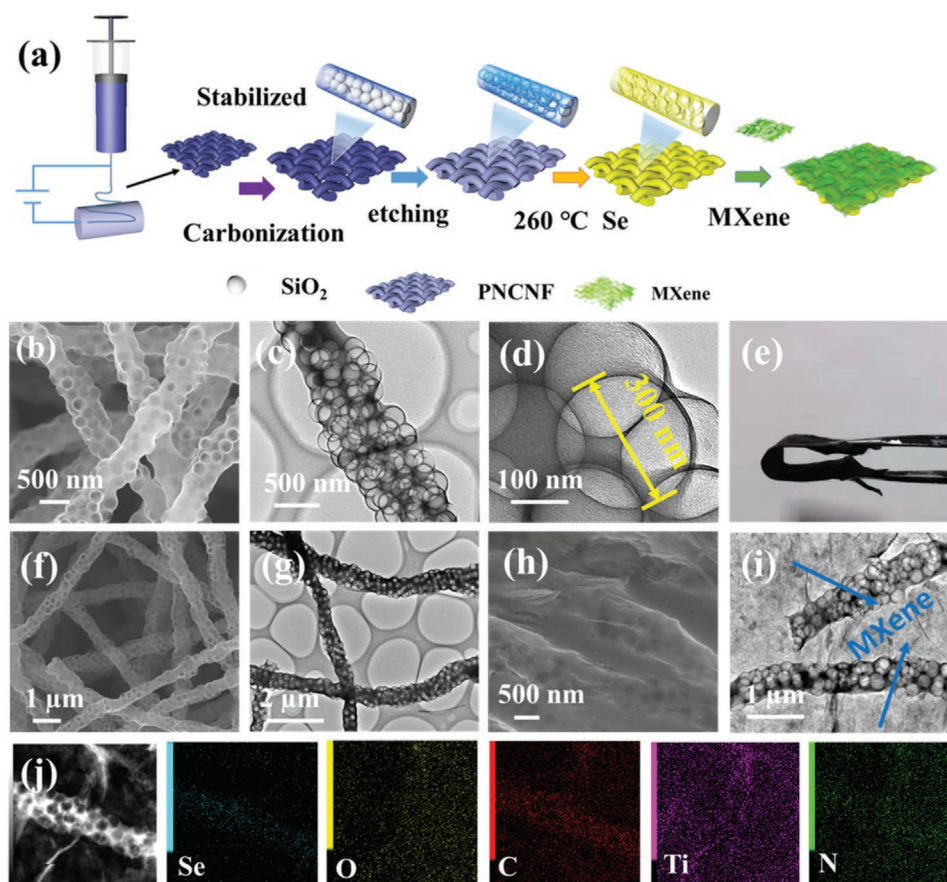E-mail: yqsu1989@xjtu.edu.cn

Figure 1. a) Schematic of the preparation process of Janus PNCNFs/Se@MXene electrode. b) SEM image of PNCNFs. c,d) TEM images of PNCNFs. e) Optical photograph of PNCNFs. f) SEM images of PNCNFs/Se. g) TEM images of PNCNFs/Se. h) SEM images of PNCNFs/Se@MXene. i) TEM images of PNCNFs/Se@MXene. j) HAADF-STEM image of PNCNFs/Se@MXene and corresponding elemental mappings.

SEM results. The microporous and mesoporous characteristics of PNCNFs were further analyzed by nitrogen adsorption–desorption isotherm measurements (Figure S5, Supporting Information). The calculated Brunauer–Emmett–Teller (BET) surface area of PNCNFs is 436.2 m^2 g^{-1}, and the pore volumes are ≈0.21 cm^3 g^{-1}. The high surface area and ample pore structure can facilitate the loading of Se and mitigate the volume variation of Se during charge/discharge.

Macroscopically, the electrodes exhibit excellent mechanical flexibility before and after etching (Figure 1e; and Figure S6, Supporting Information), hence enabling their direct integration in Na–Se and Li–Se batteries. High-angle annular dark-field scanning transmission electron microscopy (HAADF-STEM) image and corresponding elemental mapping of C, N, and O (Figure S7, Supporting Information) reveal the porous morphology and the uniform distribution of C, N, and O elements within PNCNFs. After Se infiltration, the morphology of PNCNFs remains intact and no Se agglomeration is observed on the surface of nanofibers (Figure 1f). As demonstrated in Figure 1g, TEM images exhibit a uniform distribution of the porous structure of carbon fiber. HAADF-STEM image (Figure S8, Supporting Information) and corresponding elemental mapping verified that selenium is well distributed in PNCNFs. SEM images of PNCNFs/Se@MXene (Figure 1h)

show that MXene sheets are completely covered and tightly connected with the PNCNFs/Se, which is critical for preserving the electrode's structural stability. TEM analysis confirms that MXene with a thin lamella structure is closely attached to the PNCNFs/Se (Figure 1i). Elemental mapping of Se, O, C, Ti, and N (Figure 1j), reveals that the addition of MXene does not affect the distribution of Se. In this flexible Janus structure, MXene nanosheets are expected to physically block the shuttle effect of sodium polyselenide while acting as electrical bridge connecting the fibers, essentially forming a 3D conductive network, while helping to reduce the transfer distance for ion/electrons.

X-ray diffraction (XRD) patterns of NCNFs, PNCNFs, PNCNFs/Se, and PNCNFs/Se@MXene samples are shown in Figure S9 (Supporting Information). The broad peak around 23° observed in all samples corresponds to amorphous carbon. When comparing with NCNFs and PNCNFs, the PNCNFs/Se and PNCNFs/Se@MXene samples with Se content of 74.9 wt% exhibit peaks associated with trigonal Se (in accordance with JCPDS#06-0362), the diffraction peaks of Se appear due to the presence of excess Se in a crystalline state on the carbon matrix surface after the voids of the porous carbon material are fully filled with amorphous Se.[9] On the other hand, diffraction peaks associated with the MXene phase were not detected most likely due to the trace amounts.[29,30]
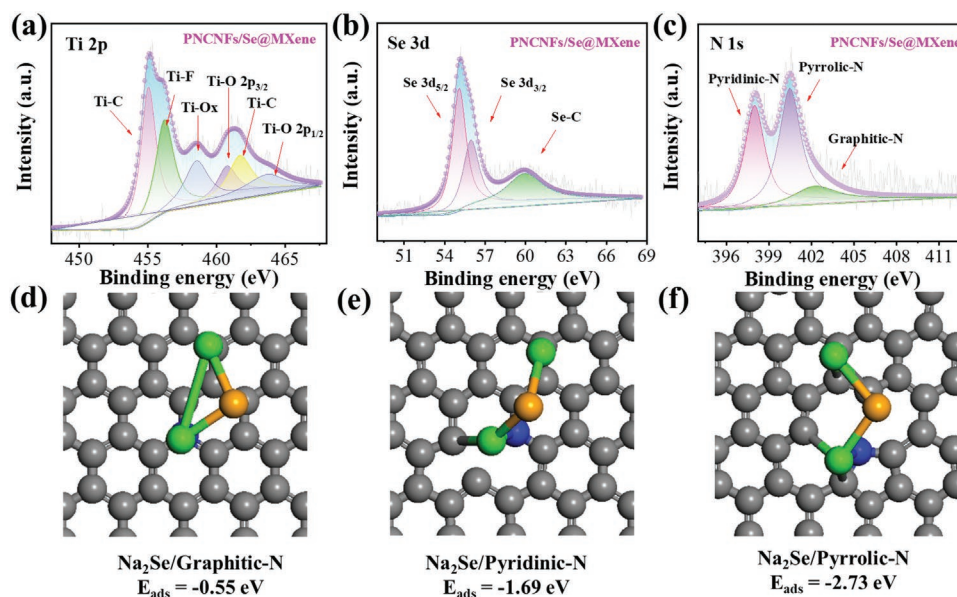
**ADVANCED
SCIENCE NEWS**

www.advancedsciencenews.com

**ADVANCED
ENERGY
MATERIALS**

www.advenergymat.de

Figure 2. a–c) High-resolution XPS spectra of Ti 2p, Se 3d, and N 1s in PNCNFs/Se@MXene. d–f) DFT calculations of the configurations and adsorption energy for Na₂Se on Graphite-N, Pyridinic-N, Pyrrolic-N in PNCNFs/Se@MXene electrode.

The chemical state and elemental composition of all samples were further analyzed by X-ray photoelectron spectroscopy (XPS). The deconvolution of N signals of PNCNFs and NCNFs is shown in Figure S10 (Supporting Information). Three main peaks located at binding energies of 398.4, 400.3, and 401.9 eV can be attributed to pyridinic-, pyrrolic-, and graphitic-N, respectively. It is worth noting that the proportion of pyrrolic-N in PNCNFs is obviously higher than that of NCNFs, which can be attributed to the production of more surfaces and defects when etching out of SiO₂ templates. It has been shown that the defects created by pyrrolic-N not only provide an embedding site for Na⁺, but also can effectively adsorb sodium polyselenide to inhibit the shuttle effect. The broad scan XPS spectrum shown in Figure S11a,d (Supporting Information) highlights that the C, N, and O are concomitant in NCNFs, and PNCNFs. The XPS survey spectrum presented in Figure S11g (Supporting Information) clearly shows that the as-synthesized PNCNFs/Se@MXene consists of Ti, Se, C, O, and N. As shown in Figure S11b,e,h (Supporting Information), the O 1s spectrum of NCNFs, PNCNFs, and PNCNFs/Se@MXene comes from various oxygen-containing groups, indicating that the O species exist in different forms. The XPS high-resolution C 1s spectrum of NCNFs, PNCNFs, and PNCNFs/Se@MXene is shown in Figure S11c,f,i (Supporting Information), which can be divided into four individual peaks corresponding to C—C/C=C (284.1 eV), C—N/C—O (284.8 eV), C—O/C=N (286.0 eV), and O=C—O (287.8 eV), respectively.

The XPS spectrum of Ti, Se, and N concomitant in the synthesized PNCNFs/Se@MXene are clearly shown in **Figure 2**. In Figure 2a, the Ti 2p spectrum of PNCNF/Se@MXene consists of four pairs of 2p₃/₂ and 2p₁/₂ doublets for Ti—C (455.1/462.0 eV) and Ti—O (460.3/464.6 eV) as well as the singlet for Ti—F (456.7 eV) and Ti—Oₓ (458.8 eV), which correspond to Ti—C functional groups, and —F and —O or —OH terminal groups on the surface of MXene.[31] Moreover, The Fourier-transform

infrared (FTIR) spectrum of PNCNFs, MXene, and PNCNFs/Se@MXene in Figure S12 (Supporting Information) also revealed that the broadband at 3360–3500 cm⁻¹ and peaks at 1560 cm⁻¹ (the yellow sign) of PNCNFs could be assigned to the stretching vibration of O—H groups originated from adsorbed water molecules. The peak at around 1190 cm⁻¹ (the green sign) is assigned as N—C stretching vibration of PNCNFs. In the FTIR spectrum of the PNCNFs/Se@MXene and Ti₃C₂Tₓ MXene, the absorption peaks at 3440 and 550 cm⁻¹ were attributed to the stretching vibration of —OH group. The peak at 1640 and 1385 cm⁻¹ was caused by the absorbance of C=O and C—F groups, which is consistent with the XPS analysis.[32,33] As illustrated in Figure 2b, the peaks located at 54.7 and 55.6 eV are ascribed to Se 3d₅/₂ and 3d₃/₂, respectively, while the peak at 59.0 eV corresponds to Se—C bonds. The mass percentage of Se in PNCNFs/Se@MXene and PNCNFs/Se composites can be estimated by thermogravimetric analysis (TG). The TG curve of PNCNFs/Se composite reveals that the Se content is 49.8 wt% (Figure S13, Supporting Information). Similarly, the N 1s can be assigned to pyridinic-, pyrrolic-, and graphitic-N (398.4, 400.3, and 401.9 eV), respectively. As shown in Figure 2c, pyrrolic-N retains a high percentage, in good agreement with the original composition of PNCNFs, and as such is expected to play a key role both in the anchoring of polyselenides and embedding of sodium ions. DFT calculations reveal higher adsorption energy of pyrrolic-N for Na₂Se (E_{ads} = −2.73 eV), which indicates pyrrolic-N has a higher adsorption ability for insoluble reactants (Figure 2d–f; and Table S1, Supporting Information). These results indicate that N-doping, especially through the increase of pyrrolic nitrogen, can significantly improve the adsorption ability for Na₂Se in the Janus structure.

The NCNFs/Se, PNCNFs/Se, and PNCNFs/Se@MXene materials were used to construct free-standing and flexible cathodes for Na–Se batteries. The electrochemical performance of the ensuing batteries is shown in **Figure 3**. Figure 3a presents
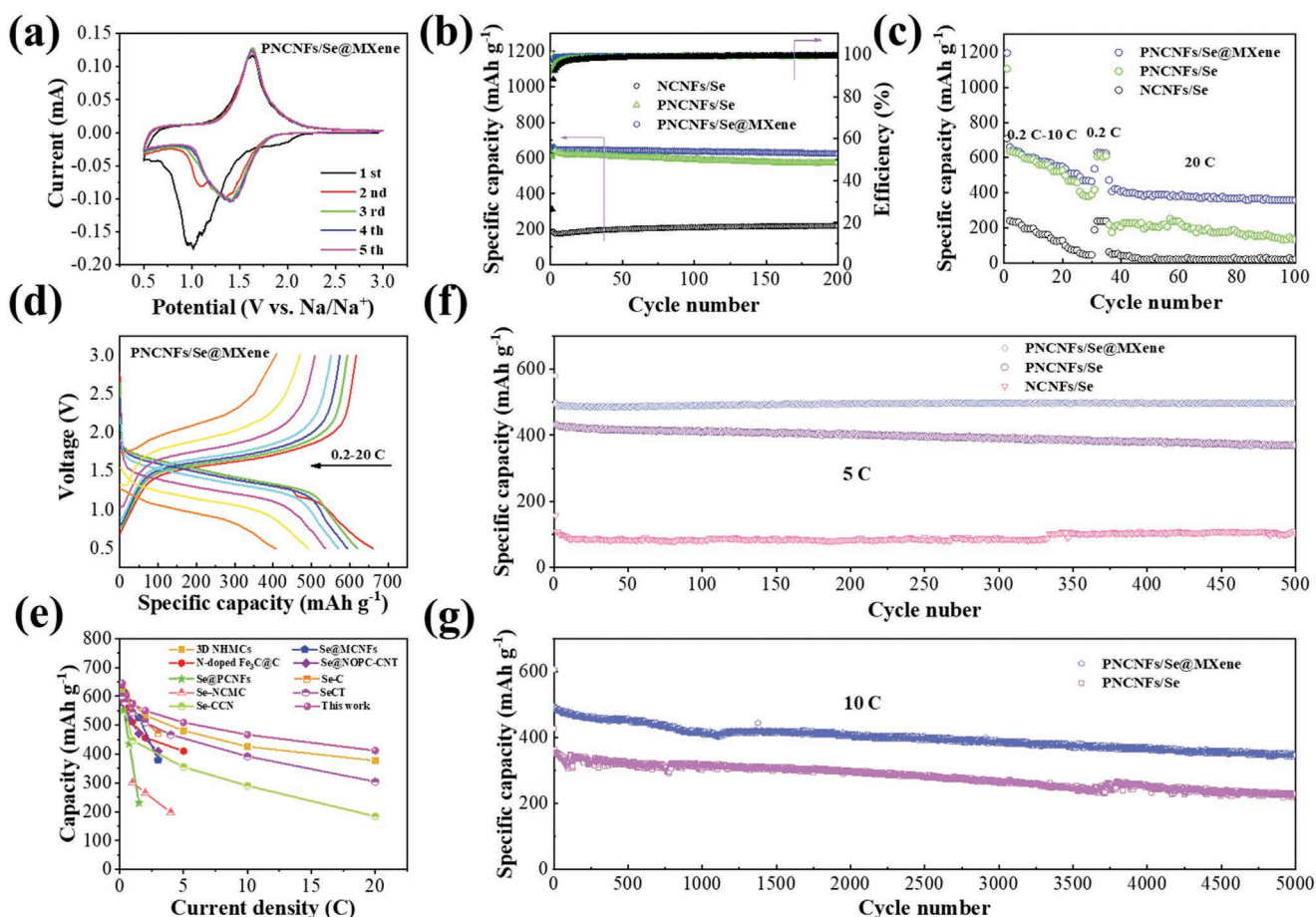
Figure 3. Electrochemical performance of PNCNFs/Se@MXene cathode in Na–Se batteries. a) CV curves of a PNCNFs/Se@MXene cathode at a scan rate of 0.1 mV s^{-1}. b) Cycling performance at 0.2 C, and c) rate capability of NCNFs/Se, PNCNFs/Se, and PNCNFs/Se@MXene electrodes. d) Charging and discharging curves for PNCNFs/Se@MXene at different C-rates. e) Comparison of rate performance among Se-based materials reported in the literature. f) Prolonged cycle life of NCNFs/Se, PNCNFs/Se, and PNCNFs/Se@MXene cathodes at 5 C rate. g) Prolonged cycle life of PNCNFs/Se, and PNCNFs/Se@MXene cathodes at 10 C rate.

cyclic voltammetry (CV) of PNCNFs/Se@MXene from 0.5 to 3.0 V, at a scan rate of 0.1 mV s^{-1}. In the first cycle, a pair of cathodic and anodic peaks are located at 1.0 and 1.64 V, correspondingly to the transformation between Se and Na$_2$Se in the carbonate-based electrolyte. From the second cycle, the cathodic peaks shift to 1.41 V and remain highly overlapped, suggesting the highly reversible cyclic property of this PNCNFs/Se@MXene cathode. Similarly, in the CV curve of cells with PNCNFs/Se cathodes (Figure S14, Supporting Information), the cathodic peak of the first cycle appears at 1.0 V and the anodic peak at 1.62 V. From the second cycle, the cathodic peak changes to 1.33 V and the cathodic and anodic peaks overlap well in subsequent cycles. Additionally, Figure S15 (Supporting Information) compares the potential difference between redox peaks of PNCNFs/Se and PNCNFs/Se@MXene cathodes at a scan rate of 0.1 mV s^{-1}. PNCNFs/Se@MXene cathodes have a smaller potential difference than NCNFs/Se, PNCNFs/Se cathodes, suggesting less polarization and faster redox kinetics.[34] The cycling performances of PNCNFs/Se@MXene, PNCNFs/Se, and NCNFs/Se cathodes at 0.2 C (1 C = 678 mA g^{-1}) are shown in Figure 3b. PNCNFs/Se@MXene cathode displays the superior performance of 625 mA h g^{-1} (based on the mass of Se)

after 200 cycles, and a low capacity loss rate of 0.028% per cycle. In comparison, PNCNFs/Se and NCNFs/Se deliver relatively low capacities of 573 and 219 mA h g^{-1} after 200 cycles, respectively. The corresponding charge–discharge curves of the above three cathodes at the 1st, 2nd, 3rd, 50th, 100th, and 200th cycles are shown in Figure S16 (Supporting Information). Note particularly that the discharge capacity of the first cycle far exceeds the theoretical specific capacity of Se because of the formation of solid-electrolyte interface (SEI) film. At the same time, Se@MXene electrodes also delivered inferior performance (only 141 mA h g^{-1} at 0.2 C after 140 cycles) to that of PNCNFs/Se@MXene electrodes owing to its stacked nonporous property (Figure S17, Supporting Information), which implies the successful design of the Janus electrode. When the areal loading of Se reaches a high value of 7.1 mg cm^{-2} (Figure S18, Supporting Information), following five cycles of activation, the cell with PNCNFs/Se@MXene electrodes still exhibits a specific capacity of 221 mA h g^{-1} at 0.5 C after 800 cycles, with a capacity decay rate of 0.0028% per cycle, demonstrating that the Janus electrode is promising to achieve stable cycling performance for high energy Na–Se batteries. When the selenium mass ratio was increased to 60% in the composite materials, the resultant

PNCNFs/Se@MXene-60% cathodes delivered 477.7 mAh g⁻¹ at 0.2 C after 200 cycles and 246.7 mAh g⁻¹ at 5 C after 500 cycles (Figure S19, Supporting Information). It is worth noting that the specific capacity of the pure PNCNFs@MXene cathode without Se loading only shows a low capacity of 16 mAh g⁻¹ at 0.2 C in the voltage range of 0.5–3.0 V (Figure S20, Supporting Information), suggesting its negligible capacity contribution for the PNCNFs/Se@MXene electrode in the charge and discharge processes.

The rate performances of the three types of cathodes were also tested (Figure 3c). Cells with PNCNFs/Se@MXene cathodes exhibited the best rate performance, with specific capacities of 645, 601, 574, 550, 509 mA h g⁻¹ at the rate of 0.2 C, 0.5 C, 1 C, 2 C, and 5 C, respectively. Even at the ultrahigh rate, they still delivered 467 and 411 mA h g⁻¹ at 10 C and 20 C, respectively. The corresponding charge–discharge platform curves of PNCNFs/Se@MXene electrodes are shown in Figure 3d. PNCNFs/Se exhibits the rate capacities of 633, 592, 559, 522, 466, 380, and 228 mA h g⁻¹, while the NCNFs/Se electrodes showed relatively low rate capacities of 240, 215, 176, 142, 98, 55, and 49 mA h g⁻¹, at 0.2 C, 0.5 C, 1 C, 2 C, 5 C, 10 C, and 20 C, respectively. Their corresponding charge–discharge curves are shown in Figure S21 (Supporting Information). Evidently, the rate ability of PNCNFs/Se@MXene cathode is far superior to those of previously reported Se-based cathode materials for Na–Se batteries (Figure 3e),[1,12,15,35–40] further highlighting the tremendous potential of the developed Janus electrode. Meanwhile, when the weight ratio of MXene is lower (named as PNCNFs/Se@MXene-L, MXene content is 0.03 mg cm⁻²) in Na–Se cells, the PNCNFs/Se@MXene-L electrode exhibits inferior electrochemical performance with specific capacities of 583, 539, 515, 490, 452, 407, 333 mAh g⁻¹ at 0.2–20 C, respectively, which could be attributed to the incomplete coating of MXene (Figure S22a, Supporting Information). When the weight ratio of MXene is higher (named as PNCNFs/Se@MXene-H, MXene content of 0.12 mg cm⁻²), the stacking MXene is not conducive to the rapid diffusion of ions in the vertical direction (Figure S22b, Supporting Information), and the PNCNFs/Se@MXene-H electrode exhibits specific capacities of 475, 452, 434, 415, 375, 335, 302 mAh g⁻¹ at 0.2–20 C, respectively, demonstrating the appropriate MXene layer can restrict the shuttle effect and enhance the electrochemical performance without restricting the ion transport.

When the current density is increased to 5 C after five cycles of activation at 0.2 C, PNCNFs/Se@MXene, PNCNFs/Se, and NCNFs/Se electrodes display the reversible specific capacities of 496, 369, and 100 mA h g⁻¹ after 500 cycles (Figure 3f), respectively. It is worth noting that PNCNFs/Se@MXene cathodes retained an ultralow capacity attenuation of only 0.0025% per cycle. In Figure 3g, after activating five cycles at 0.2 C, PNCNFs/Se@MXene exhibits 348 mA h g⁻¹ at 10 C after 5000 long-term cycles with a capacity decay as low as 0.0059% per cycle, superior to the PNCNFs/Se electrode with a capacity of 226 mA h g⁻¹ at 10 C after 5000 cycles and a decay rate of 0.0073%, further demonstrating the outstanding cycling stability and high-rate performance of the PNCNFs/Se@MXene cathodes. The introduction of MXene not only boosts the adsorption of polyselenides, but also provides a physical barrier for the shuttle of polyselenides. The admirable long-term cycling performance of PNCNFs/Se@MXene electrodes at high current densities is superior compared to previously reported cathode materials in Na–Se batteries (Table S2, Supporting Information).[1,12,15,16,18,35–38,41–45]

To further understand the electrochemical characteristics of NCNFs/Se, PNCNFs/Se, and PNCNFs/Se@MXene in Na–Se batteries, the electrochemical kinetics was studied via CV measurements in the scanning rate range of 0.1–0.5 mV s⁻¹. As shown in **Figure 4**a, there are two characteristic peaks (denoted as Peak O and Peak R). Compared with Figures S23a and S24a (Supporting Information), PNCNFs/Se@MXene cathodes show higher current density than NCNFs/Se and PNCNFs/Se cathodes, indicating fast electrochemical kinetics of PNCNFs/Se@MXene cathodes. The relationship between voltage scanning rate (v) and the corresponding peak current (i) can be applied to distinguish the capacity contribution, according to $\log(i) = \log(a) + b\log(v)$, where a is a constant, and b is the power-law exponent. The value of b (slope) is a key parameter for the analysis of reaction kinetics. While the value of b is close to 0.5, a diffusion-controlled process is dominating the electrochemical reaction. When the b value is between 0.5 and 1.0, a mix of diffusion-controlled and capacitive processes are dominating response, and when the b value is closer to 1.0, capacitive behavior is dominant, accompanied by faster kinetics. From Figure 4b; and Figures S23b and S24b (Supporting Information), the fitting values for b indicate that PNCNFs have effectively improved reaction kinetics of electrochemical reactions as a result of exposure to more surfaces area and the presence of pyrrolic-N. Figure 4c; and Figures S23c and S24c (Supporting Information) reveal that 93.5%, 91.7%, and 83.9% of the total capacity is contributed by a capacitive process at a scan rate of 0.5 mV s⁻¹ for PNCNFs/Se@MXene, PNCNFs/Se, and NCNFs/Se electrodes, respectively. As shown in Figure 4d; and Figures S23d and S24d (Supporting Information), it is found that the relative proportion of capacitance contribution to the total capacity gradually increases with increasing scan rate. In general, capacitive behavior is closely related to the electrochemical kinetics of battery electrodes. Therefore, a high ratio of capacitive-controlled process predicts a rapid transport of Na⁺ in battery electrodes, which would lead to superior rate and long cycling performance of cells.

The galvanostatic intermittent titration (GITT) profiles for NCNFs/Se, PNCNFs/Se, and PNCNFs/Se@MXene electrodes are shown in Figure 4e; and Figure S25 (Supporting Information). These data allow assessment of the polarization phenomena in the redox reactions. To this end, we note that the voltage changes during Na⁺ intercalation process in PNCNFs/Se@MXene are smaller than those in NCNFs/Se and PNCNFs/Se, suggesting better reaction kinetics in the PNCNFs/Se@MXene. Figure S26 (Supporting Information) shows the sodium ion diffusion coefficient of PNCNFs/Se@MXene, PNCNFs/Se, and NCNFs/Se from the GITT curves. The Na-ion diffusion coefficient of the PNCNFs/Se@MXene electrode has the value between 3.9×10^{-13} and 1.2×10^{-9} cm² s⁻¹, while that of the PNCNFs/Se and NCNFs/Se electrode lies at 7.8×10^{-14}–2.6×10^{-11}, 3.5×10^{-14}–8.5×10^{-11} cm² s⁻¹, respectively. Obviously, the Na-ion diffusion coefficient of the PNCNFs/Se@MXene and PNCNFs/Se electrode is higher than that of the NCNFs/Se electrode in each of the same sodiation or desodiation states.
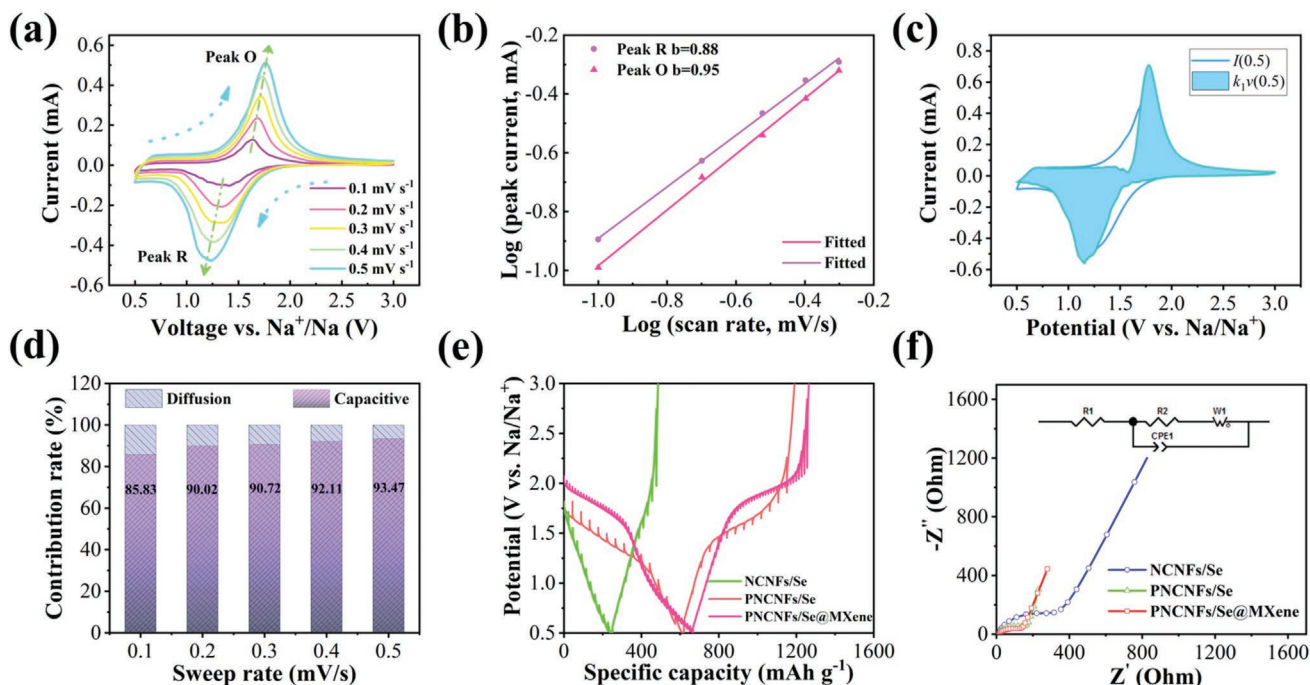
**ADVANCED
SCIENCE NEWS**

www.advancedsciencenews.com

**ADVANCED
ENERGY
MATERIALS**

www.advenergymat.de

Figure 4. a) CV curves of PNCNFs/Se@MXene from 0.1 to 0.5 mV s^{-1}. b) Corresponding linear fitting plots of peak currents versus scan rates of PNCNFs/Se@MXene. c) Capacitance contribution fitting diagram at 0.5 mV s^{-1}. d) Contribution ratio of the capacitive process at 0.1–0.5 mV s^{-1} for a PNCNFs/Se@MXene cathode. e) GITT profiles of NCNFs/Se, PNCNFs/Se, and PNCNFs/Se@Mxene electrodes. f) EIS of test cells with different cathodes before cycling.

This higher Na-ion diffusion rate of the PNCNFs/Se@MXene supports a superior rate capability. Electrochemical impedance spectroscopy (EIS) measurements were also conducted to study the overall electrical effects of changes in reaction kinetics (Figure 4f). The resistance values obtained from the typical Nyquist plots of three samples were displayed in Table S3 (Supporting Information). PNCNFs/Se@MXene electrode exhibits the smallest R_{ct} values (R_{ct}: electron transfer resistance on electrode surface), indicating a significant improvement of charge transfer kinetics upon MXene incorporation.

To study the effect of NaPSe on the electrodes, NCNFs/Se, PNCNFs/Se, and PNCNFs/Se@MXene cathodes were employed to assemble optically transparent electrochemical test cells. Although the electrolyte in all three types of cells initially appears clear (**Figure 5**a), after 8 h of discharging, the electrolyte in the NCNFs/Se cell develops a light brown coloration while the Na metal develops a pale yellow appearance. Both observations could be ascribed to the diffusion of soluble NaPSe. On the contrary, in cells incorporating PNCNFs/Se and PNCNFs/Se@MXene, there were no obvious changes either in the electrolyte or the anodes or cathodes, verifying the effective blocking of NaPSe diffusion and reactions. The latter is a critical characteristic of the PNCNFs/Se@MXene cathodes as it mitigates the shuttle effect and improves the rate performance and cycle stability of the ensuing cells.

To further understand the underlying mechanisms responsible for the superior cyclic stability and high-rate ability of the cells, we have also investigated the adsorption behavior of NaPSe on Ti$_3$C$_2$T$_x$ MXene with a different group (−O, −F, −OH) using DFT calculations. As shown in Figure 5b–d; and

Table S4 (Supporting Information), the adsorption energies of MXene with −O, −OH, and −F groups for Na$_2$Se are −6.38, −6.45, and −5.57 eV, respectively, which possesses stronger adsorption energy than that of PNCNFs (the maximum adsorption energy is that of pyrrolic-N for Na$_2$Se, −2.73 eV), proving that MXene layer with different functional groups (−OH, −F, −O) on the surface could reduce the loss of active substances and ensure reversible conversion process during charging and discharging process. Meanwhile, the adsorption energies of MXene with −O, −OH, and −F group to Na$_2$Se$_4$ are −4.59, −8.83, and −5.54 eV, respectively, and the adsorption energies of PNCNFs with pyrrolic-N to Na$_2$Se$_4$ is −1.19 eV, which shows stronger adsorption energy than that of DMC and EC solvent molecule in electrolyte (E_{ads} for DMC is −0.47 eV, E_{ads} for EC is −0.51 eV) in Figure S27 (Supporting Information). The results indicate that the polyselenide prefers remain in the cathode instead of dissolving into the electrolyte, thus achieving the inhibition of the shuttle effect of polyselenide by the designed electrode.

Therefore, 2D Ti$_3$C$_2$T$_x$ MXene on PNCNFs/Se@MXene cathode could alleviate the shuttle effect of polyselenides and minimize reaction energy barriers, together with its physical barrier function, leading to higher selenium utilization, superior cycling ability, and high rate capability. Furthermore, we disassembled the separators from NCNFs/Se, PNCNFs/Se, and PNCNFs/Se@MXene cathode cells after 500 charge–discharge cycles and studied their optical appearance. For the cell based on NCNFs/Se, the separators appear yellow (Figure S28, Supporting Information). This is not the case for cells based on PNCNFs/Se and PNCNFs/Se@MXene cathodes in which the
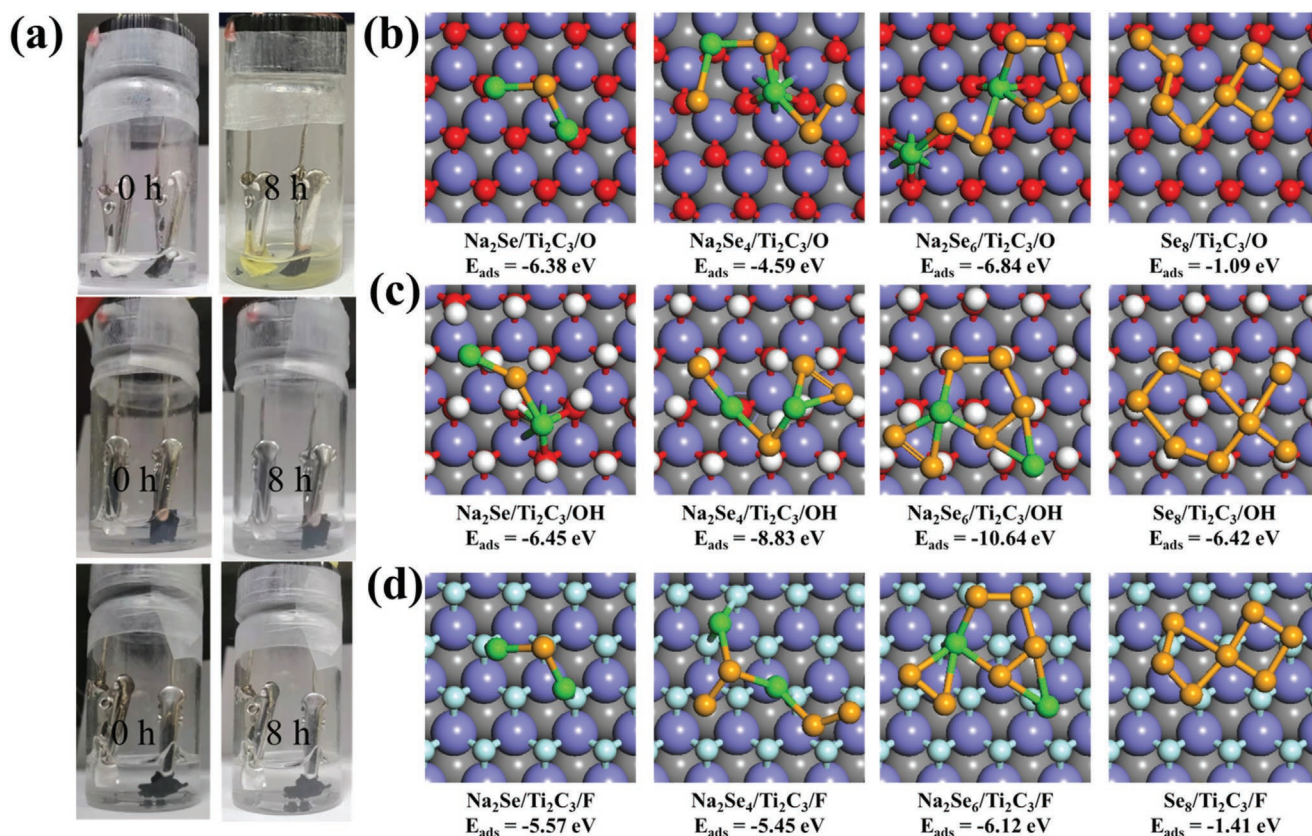
**ADVANCED
SCIENCE NEWS**

www.advancedsciencenews.com

**ADVANCED
ENERGY
MATERIALS**

www.advenergymat.de

Figure 5. a) Photographs of transparent test cells of NCNFs/Se, PNCNFs/Se, and PNCNFs/Se@MXene during charge/discharge cycling. b–d) DFT calculations of the configurations and adsorption energy for sodium polyselenides on MXene with F, O, and OH groups. The blue, gray, yellow, green, wathet, red, and white balls represent Ti, C, Se, Na, F, O, and H atoms, respectively.

separators retain their original color/appearance, further supporting our hypothesis that the incorporation of $Ti_3C_2T_x$ MXene helps to reduce the shuttle effect of polyselenide and enhance its adsorption with increasing pyrrolic-N concentration.

In order to gain insight into the mechanism and high kinetics of PNCNFs/Se@MXene electrode, in situ XRD was performed to investigate the charge/discharge products and intermediate phases of the Na-PNCNFs/Se@MXene cells. As illustrated in **Figure 6**a, the typical trigonal Se characteristic peak gradually wear off during discharging to 0.5 V. meanwhile, the peak of Na_2Se discharge product at 44.1° started to occur and the intensity gradually increased around 0.5 V. When the cell was charged in the reverse process, the peak of Na_2Se began to fade out and the peak of Se intensity gradually increased until 3.0 V, indicating that the discharge product was reoxidized into the chain-like Se molecules. The broad peak around 23° observed in whole charging and discharging process corresponds to amorphous carbon. And the peaks located at 45° and 46° is attributed to Al and Be. Figure 6b shows a conceptual diagram about the role of Janus PNCNFs/Se@MXene in a Na–Se cell, and the excellent performance may be attributed to the following key factors: 1) PNCNFs facilitate effective storage of the active substance by alleviating issues associated with volume change and increasing the active area with better ions accessibility, 2) pyrrolic-N exhibits strong adsorption toward polyselenide and speeds up the reaction kinetics, 3) 2D MXene with

polar interfaces enables the strong chemical immobilization of polyselenide and further physically blocks polyselenide to suppress shuttle effect, and 4) the characteristic 3D interconnected electrode structure enhances both electron transport and the contact area with mobile ions of interest.

The lithium storage behavior of the free-standing PNCNFs/Se@MXene electrodes with a Se content of 74.9 wt% was also investigated (Figure S29, Supporting Information). **Figure 7**a shows the CV curves for Li–Se batteries of PNCNFs/Se@MXene in the range of 1.0–3.0 V. Except for the first cycle, the following curves overlap well, proving the reversibility of the charge–discharge cycles. Figure 7b shows Li–Se batteries with PNCNFs/Se@MXene cathodes, exhibiting a specific capacity of 429 mA h g^{-1} at 0.2 C after 200 cycles. The initial discharge and charge capacities are 811 and 520 mA h g^{-1}, respectively, with an initial CE of 64.2%. The corresponding charge/discharge profiles at 0.2 C are shown in Figure S30 (Supporting Information). The specific capacity retention characteristics at different C-rates are shown in Figure 7c. The corresponding capacity values are 428, 394, 372, 349, 317, 293, and 266 mAh g^{-1} for 0.2 C, 0.5 C, 1, 2 C, 5 C, 10 C, and 20 C (1 C = 678 mA g^{-1}), respectively. The corresponding charge/discharge profiles at 0.2–20 C for Li–Se batteries are shown in Figure 7d. Furthermore, compared with state-of-the-art Se-based materials (Table S5, Supporting Information),[5,38,46–52] Li–Se batteries with flexible PNCNFs/Se@MXene electrodes subjected to long-cycling at

**ADVANCED
SCIENCE NEWS**

www.advancedsciencenews.com

**ADVANCED
ENERGY
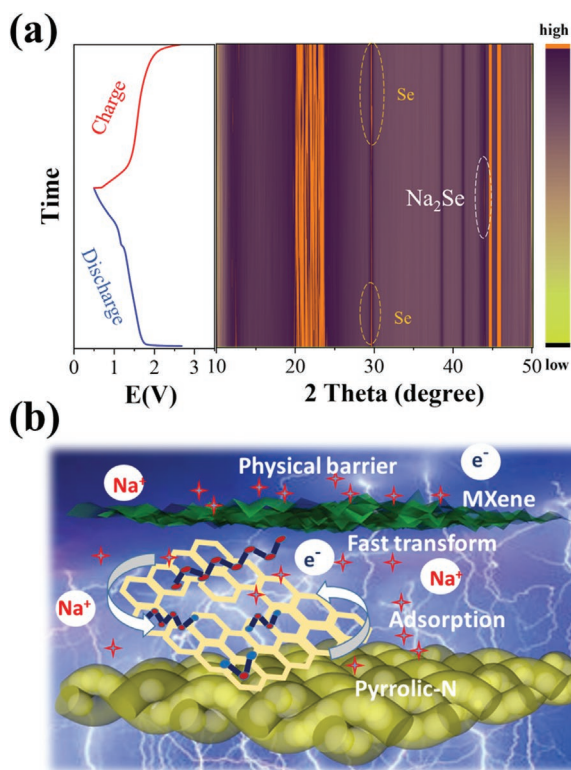MATERIALS**

www.advenergymat.de

Figure 6. a) Contour plot of the in-situ XRD of PNCNFs/Se@MXene in Na–Se batteries. b) Conceptual views of the Janus PNCNFs/Se@MXene electrode.

5 C exhibits an excellent specific capacity of 298 mAh g^{-1} after 3500 cycles (after initial 5 cycles activation at 0.2 C) (Figure 7e), demonstrating its tremendous potential for Li–Se battery applications.

3. Conclusion

In summary, we designed and developed a flexible Janus PNCNFs/Se@MXene cathode electrode for application in Na–Se and Li–Se batteries. This unique Janus structure enables the cathodes a synergistic multifunctional effect. The PNCNFs with porous structure and abundant exposed pyrrolic-N facilitate effective storage of the active substance and increase the active area with better ions accessibility synchronously strong adsorption toward polyselenide to speed up the reaction kinetics. 2D MXene with polar interfaces enables the strong chemical immobilization and further physically blocks polyselenide to suppress the shuttle effect, and the characteristic 3D interconnected electrode structure enhances both electron transport and the contact area with mobile ions of interest. The resulting Na–Se batteries utilizing the PNCNFs/Se@MXene cathode exhibit a reversible capacity up to 348 mA h g^{-1} at 10 C after 5000 cycles. Even at 20 C, the PNCNFs/Se@MXene-based cells can retain a capacity of 411 mA h g^{-1}. In the case of Li–Se batteries, the cells exhibit a long-term capacity of 298 mA h g^{-1} after 3500 cycles at 5 C at a high Se loading of 74.9 wt%. This work provides many opportunities and profound inspiration for

the future design of MXene-based flexible cathodes in Na–Se and Li–Se batteries and could be easily expanded to other low-dimensional materials for advanced energy storage systems.

4. Experimental Section

Chemicals: DMF, Tetraethyl orthosilicate (TEOS), ammonium hydroxide (NH$_3$ H$_2$O), HF, ethanol, deionized water, and selenium powder, Lithium fluoride (LiF), Hydrochloric acid (HCl). All reagents were used without further purification.

MXene Suspension Synthesis: Ti$_3$C$_2$T$_x$ MXene suspension was prepared by LiF/HCl etching Ti$_3$AlC$_2$ (11 technology Co., Ltd), and then exfoliation. The concentration of Ti$_3$C$_2$T$_x$ MXene suspension used was 2 mg mL^{-1}.

Silica (SiO$_2$) Spheres Template Synthesis: The TEOS solution was added into a mixed solution consisting of 75 mL alcohol, 10 mL deionized water, and 3.15 mL NH$_3$ H$_2$O. After stirring for 1 h at room temperature, the SiO$_2$ spheres were centrifuged and cleaned with deionized water and ethanol. The SiO$_2$ spheres were dried at 60 °C for a night.

Synthesis of PNCNFs/Se: In a typical process, 0.6 g PAN (polyacrylonitrile M_W = 150 000, Aldrich), 3 g DMF, and 0.5 g SiO$_2$ were stirred at room temperature to form a well-distributed precursor solution. The solution was transferred to a 5 mL syringe for electrospinning at a feed rate of 10 µL min^{-1} when the voltage was 23 kV between positive and negative, the distance was 15 cm from the aluminum foil collector. The as-spun nanofiber was dried all night at 60 °C, annealed in air at 260 °C for 2 h, and then carbonized in Ar atmosphere at 800 °C for 2 h with a heating rate of 1 °C min^{-1}. Finally, the obtained film was etched in 5% HF aqueous solution overnight to eliminate the SiO$_2$ and washed with deionized water until pH neutrality was reached. After drying in a vacuum drying chamber at 60 °C for a night, the obtained PNCNF mats were cut into small pieces and mixed with Se powder heat at 260 °C for 2 h in a sealed container with an Ar atmosphere. After cooling down naturally, PNCNFs/Se was obtained. As a control, NCNFs were prepared under the same conditions except for omitting the addition of SiO$_2$. Different selenium load was controlled by adding different selenium powder.

Synthesis of PNCNFs/Se@MXene Electrodes: The above MXene suspension was diluted in a 1:1 mixture of water and ethanol, then dropped onto PNCNFs/Se electrodes. After drying at a low temperature of 35 °C under a vacuum state, the PNCNFs/Se@MXene electrodes with a trace MXene loading of 0.057 mg cm^{-2} were obtained. The amount of MXene can be controlled by the drip. PNCNFs/Se@MXene-L electrodes with MXene content of 0.03 mg cm^{-2} and PNCNFs/Se@MXene-H electrodes with MXene content of 0.12 mg cm^{-2} were prepared.

Materials Characterization: XRD (Cu Ka radiation, 0.154 nm) measurements were used to analyze the structural and component information of composites scanning from 5° to 70°. SEM (Nova Nano SEM450, operated at 15 keV) and TEM (JEOL JEM 2100F) were employed to characterize the morphologies and structures of the composites. The elemental distribution was analyzed by EDS attached to the HRTEM (Oxford Instrument and EDAX Inc). XPS (ESCALAB 250) was carried out by Al K$_\alpha$ X-ray source at 14 kV. TG (Q5000IR America) was used to test the selenium content of PNCNFs/Se under N$_2$ heating from room temperature to 800 °C at a rate of 1 °C min^{-1}. Nitrogen adsorption/desorption isotherms measurements were conducted at 77 K with a Tristar 3000. FT-IR spectra were obtained using a Nicolet iS50 FT-IR spectrometer (Thermo Fisher Scientific) with the wavenumber ranging from 400 to 4000 cm^{-1}. In situ XRD (Bruker D8 advance) measurements were used to analyze the structural and component information of composites during charge and discharge scanning from 5° to 50°. The in situ XRD electrode was assembled in a battery mold with a Be window, and the cathodes material is ground into powder and coated on aluminum foil, and the counter electrode and the separator were the same size as the coin-cells.

Electrochemical Characterization: The free-standing PNCNFs/Se@MXene (or PNCNFs/Se, NCNFs/Se) electrodes were directly used as
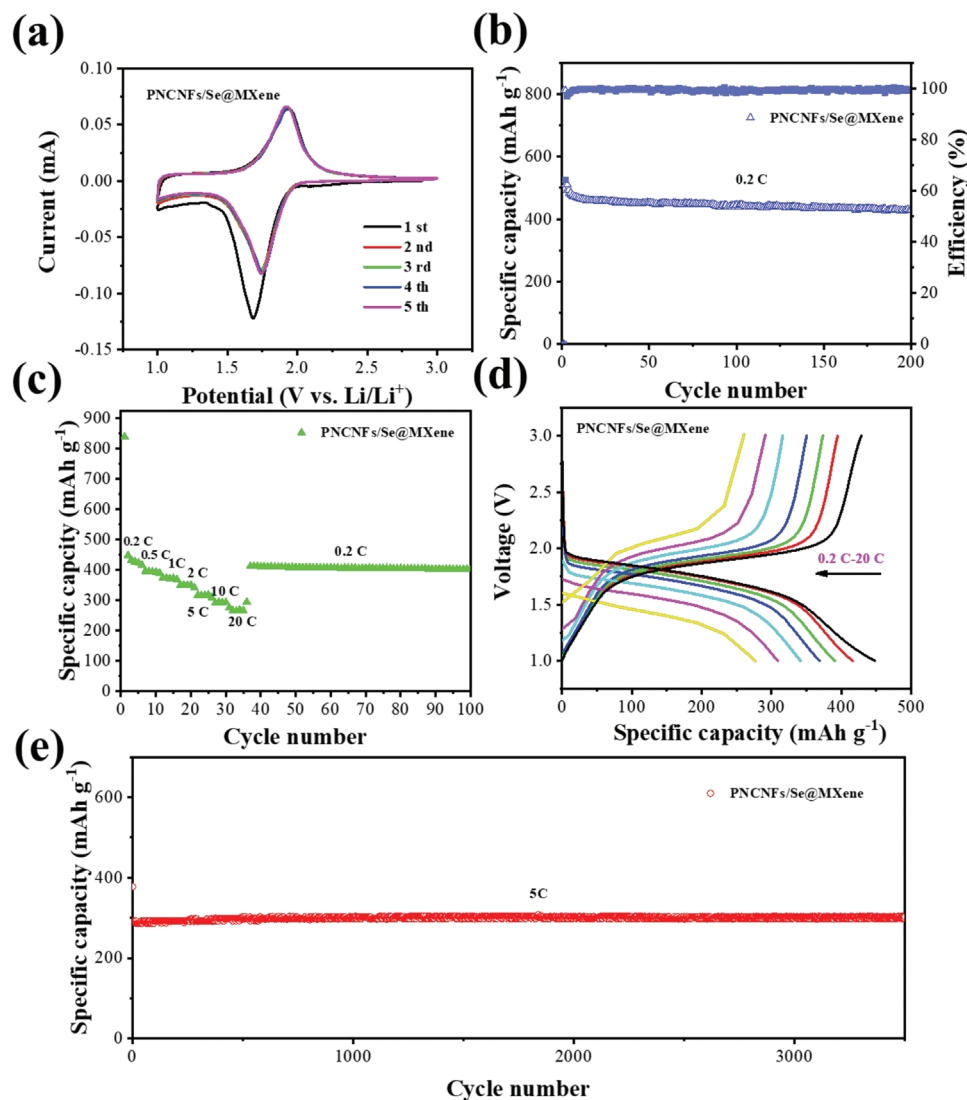
Figure 7. Electrochemical performance of a PNCNFs/Se@MXene cathode in a Li–Se test battery. a) CV curves of a PNCNFs/Se@MXene cathode at 0.1 mV s⁻¹. b–d) PNCNFs/Se@MXene cycling performance, rate capability, charge–discharge curves at different C-rates. e) Prolonged cycle life of PNCNFs/Se@MXene cathode at a 5 C rate.

working electrodes, Na metal (or Li metal) as counter electrodes, and Glass fiber (Whatman) (or PP) was used for separator films. For Na–Se batteries, 1 M $NaClO_4$ in ethylene carbonate-dimethyl carbonate (W_{EC}: W_{DMC} = 1:1) was used as the electrolyte, with 50 µL of electrolyte used per cell. For Li–Se batteries, the electrolyte was 1 M $LiPF_6$ in ethylene carbonate (EC) and diethyl carbonate (DEC) (V_{EC}:V_{DEC} = 1:1), with 20 µL amount of electrolyte used per cell. CR2032 coin cells were constituted in a glove box filled with argon gas. The areal Se areal loading in Na–Se (or Li–Se) is about 0.8–1.2 mg cm⁻². Galvanostatic charge–discharge was tested at 25 °C in a voltage range from 0.5 to 3 V (1–3 V for Li-Se) on LAND system. The cyclic voltammetry (CV) measurements with a scan rate of 0.1 mV s⁻¹ and electrochemical impedance spectroscopy (EIS) with an applied amplitude of 5 mV over the frequency from 1 mHz to 100 kHz were conducted on a CHI 660E workstation. The specific capacities of all samples in Na–Se or Li–Se batteries are based on the mass of active Se loading.

DFT Calculations: Spin-polarized calculations within the density-functional theory framework were carried out as implemented in the Vienna ab initio simulation package (VASP).[53] The ion-electron interactions were represented by the projector-augmented wave (PAW)

method[54] and the electron exchange-correlation by the generalized gradient approximation (GGA) with the Perdew–Burke–Ernzerhof (PBE) exchange-correlation functional.[55] The Kohn–Sham valence states were expanded on a plane-wave basis set with cut-off energy of 400 eV. The empirical DFT-D3 correction was contained for the weak van der Waals interaction for all calculations.[56] A 3 × 3 supercell of Ti_3C_2 was employed to mimic MXene with decoration by F and OH groups. A 6 × 6 supercell of graphene with N doping was adopted to model graphitic, pyridinic, and pyrrolic N sites. For the Brillouin zone integration, a 5 × 5 × 1 Monkhorst–Pack mesh was used. All atoms were allowed to relax. The geometry optimization was performed when the convergence criterion on forces became smaller than 0.02 eV Å⁻¹ and the energy difference was <10⁻⁵ eV.

Supporting Information

Supporting Information is available from the Wiley Online Library or from the author.

Conflict of Interest

The authors declare no conflict of interest.

Data Availability Statement

The data that support the findings of this study are available from the corresponding author upon reasonable request.

Keywords

Janus electrode, Li–Se batteries, MXene, Na–Se batteries, pyrrolic-N

[1] J. Ding, H. Zhou, H. Zhang, T. Stephenson, Z. Li, D. Karpuzov, D. Mitlin, *Energy Environ. Sci.* **2017**, *10*, 153.

[2] J. Li, H. Zhang, L. Luo, H. Li, J. He, H. Zu, L. Liu, H. Liu, F. Wang, J. Song, *J. Mater. Chem. A* **2021**, *9*, 2205.

[3] X. L. Huang, C. Zhou, W. He, S. Sun, Y.-L. Chueh, Z. M. Wang, H. K. Liu, S. X. Dou, *ACS Nano* **2021**, *15*, 5876.

[4] J. Sun, Z. Du, Y. Liu, W. Ai, K. Wang, T. Wang, H. Du, L. Liu, W. Huang, *Adv. Mater.* **2021**, *33*, 2003845.

[5] C. Luo, J. Wang, L. Suo, J. Mao, X. Fan, C. Wang, *J. Mater. Chem. A* **2015**, *3*, 555.

[6] L. Wang, X. Zhang, L. Deng, J. Tang, H. Deng, W. Hu, Z. Liu, *ACS Appl. Mater. Interfaces* **2019**, *11*, 4995.

[7] J. K. Kim, Y. C. Kang, *ACS Nano* **2020**, *14*, 13203.

[8] M. H. A. Shiraz, H. Zhu, J. Liu, *J. Mater. Res.* **2020**, *35*, 747.

[9] X. Zhao, L. Yin, T. Zhang, M. Zhang, Z. Fang, C. Wang, Y. Wei, G. Chen, D. Zhang, Z. Sun, F. Li, *Nano Energy* **2018**, *49*, 137.

[10] W. Dong, H. Chen, F. Xia, W. Yu, J. Song, S. Wu, Z. Deng, Z.-Y. Hu, T. Hasan, Y. Li, H. Wang, L. Chen, B.-L. Su, *J. Mater. Chem. A* **2018**, *6*, 22790.

[11] P. Lu, F. Liu, F. Zhou, J. Qin, H. Shi, Z.-S. Wu, *J. Energy Chem.* **2021**, *55*, 476.

[12] X. Hu, J. Li, G. Zhong, Y. Liu, J. Yuan, S. Lei, H. Zhan, Z. Wen, *Small* **2020**, *16*, 2005534.

[13] H. Tian, H. Tian, S. Wang, S. Chen, F. Zhang, L. Song, H. Liu, J. Liu, G. Wang, *Nat. Commun.* **2020**, *11*, 5025.

[14] H. Huang, X. Luo, Y. Yao, X. Zhou, X. Jiang, C. Guo, J. Liu, X. Wu, Y. Yu, *InfoMat* **2021**, *3*, 421.

[15] Y. Yao, M. Chen, R. Xu, S. Zeng, H. Yang, S. Ye, F. Liu, X. Wu, Y. Yu, *Adv. Mater.* **2018**, *30*, 1805234.

[16] Q. Xu, H. Liu, W. Du, R. Zhan, L. Hu, S. Bao, C. Dai, F. Liu, M. Xu, *Electrochim. Acta* **2018**, *276*, 21.

[17] S. Kim, M. Cho, Y. Lee, *Adv. Energy Mater.* **2020**, *10*, 1903477.

[18] F. Zhang, P. Xiong, X. Guo, J. Zhang, W. Yang, W. Wu, H. Liu, G. Wang, *Energy Storage Mater.* **2019**, *19*, 251.

[19] D. Ma, Y. Li, J. Yang, H. Mi, S. Luo, L. Deng, C. Yan, P. Zhang, Z. Lin, X. Ren, J. Li, H. Zhang, *Nano Energy* **2018**, *43*, 317.

[20] J. X. Nan, X. Guo, J. Xiao, X. Li, W. H. Chen, W. J. Wu, H. Liu, Y. Wang, M. H. Wu, G. X. Wang, *Small* **2019**, *1902085*, 20.

[21] C. Lu, A. Li, G. Li, Y. Yan, M. Zhang, Q. Yang, W. Zhou, L. Guo, *Adv. Mater.* **2021**, *33*, 2008414.

[22] S. Kajiyama, L. Szabova, K. Sodeyama, H. Iinuma, R. Morita, K. Gotoh, Y. Tateyama, M. Okubo, A. Yamada, *ACS Nano* **2016**, *10*, 3334.

[23] Y. Zhang, Z. Mu, C. Yang, Z. Xu, S. Zhang, X. Zhang, Y. Li, J. Lai, Z. Sun, Y. Yang, Y. Chao, C. Li, X. Ge, W. Yang, S. Guo, *Adv. Funct. Mater.* **2018**, *28*, 1707578.

[24] J. J. Song, X. Guo, J. Q. Zhang, Y. Chen, C. Y. Zhang, L. Q. Luo, F. Y. Wang, G. X. Wang, *J. Mater. Chem. A* **2019**, *7*, 6507.

[25] J. J. Song, D. W. Su, X. Q. Xie, X. Guo, W. Z. Bao, G. J. Shao, G. X. Wang, *ACS Appl. Mater. Interfaces* **2016**, *8*, 29427.

[26] X. Liang, A. Garsuch, L. F. Nazar, *Angew. Chem., Int. Ed.* **2015**, *54*, 3907.

[27] J. Feng, Y. Li, J. Yuan, Y. Zhao, J. Zhang, F. Y. Wang, J. Tang, J. J. Song, *Front. Chem.* **2022**, *9*, 830485.

[28] F. Zhang, X. Guo, P. Xiong, J. Q. Zhang, J. J. Song, K. Yan, X. C. Gao, H. Liu, G. X. Wang, *Adv. Energy Mater.* **2020**, *10*, 2000446.

[29] W. Bao, L. Liu, C. Wang, S. Choi, D. Wang, G. Wang, *Adv. Energy Mater.* **2018**, *8*, 1702485.

[30] B. Soundiraraju, B. K. George, *ACS Nano* **2017**, *11*, 8892.

[31] K. Liu, H. Zhang, T. Fu, L. Wang, R. Tang, Z. Tong, X. Huang, *Chem. Eng. J.* **2022**, *438*, 135609.

[32] L. Wang, L. Chen, P. Song, C. Liang, Y. Lu, H. Qiu, Y. Zhang, J. Kong, J. Gu, *Composites, Part B* **2019**, *171*, 111.

[33] Y. Jeon, J.-I. Park, J. Ok, A. Dorjgotov, H.-J. Kim, H. Kim, C. Lee, S. Park, Y.-G. Shul, *Int. J. Hydrogen Energy* **2016**, *41*, 6864.

[34] W. Yang, J. Zhou, S. Wang, W. Zhang, Z. Wang, F. Lv, K. Wang, Q. Sun, S. Guo, *Energy Environ. Sci.* **2019**, *12*, 1605.

[35] J. Ding, H. Zhou, H. Zhang, L. Tong, D. Mitlin, *Adv. Energy Mater.* **2018**, *8*, 1701918.

[36] B. Yuan, X. Sun, L. Zeng, Y. Yu, Q. Wang, *Small* **2018**, *14*, 1703252.

[37] H. Wang, Y. Jiang, A. Manthiram, *Energy Storage Mater.* **2019**, *16*, 374.

[38] L. Zeng, W. Zeng, Y. Jiang, X. Wei, W. Li, C. Yang, Y. Zhu, Y. Yu, *Adv. Energy Mater.* **2015**, *5*, 1401377.

[39] M. H. A. Shiraz, P. Zhao, J. Liu, *J. Power Sources* **2020**, *453*, 227855.

[40] X. Yang, H. Wang, D. Y. W. Yu, A. L. Rogach, *Adv. Funct. Mater.* **2018**, *28*, 1706609.

[41] T. Wu, Z. Ding, M. Jing, G. Zou, H. Hou, Y. Tian, Y. Jiang, W. Hong, X. Ji, *Adv. Funct. Mater.* **2019**, *29*, 1809014.

[42] Q. Xu, T. Yang, W. Gao, R. Zhan, Y. Zhang, S. Bao, X. Li, Y. Chen, M. Xu, *J. Power Sources* **2019**, *443*, 227245.

[43] L. Zeng, X. Wei, J. Wang, Y. Jiang, W. Li, Y. Yu, *J. Power Sources* **2015**, *281*, 461.

[44] C. Ma, H. Wang, X. Zhao, X. Wang, Y. Miao, L. Cheng, C. Wang, L. Wang, H. Yue, D. Zhang, *Energy Technol.* **2020**, *8*, 1901445.

[45] R. Qiu, R. Fei, T. Zhang, X. Liu, J. Jin, H. Fan, R. Wang, B. He, Y. Gong, H. Wang, *Electrochim. Acta* **2020**, *356*, 136832.

[46] S. K. Park, J. S. Park, Y. C. Kang, *ACS Appl. Mater. Interfaces* **2018**, *10*, 16531.

[47] S.-K. Park, J.-S. Park, Y. C. Kang, *J. Mater. Chem. A* **2018**, *6*, 1028.

[48] Y. Liu, L. Si, X. Zhou, X. Liu, Y. Xu, J. Bao, Z. Dai, *J. Mater. Chem. A* **2014**, *2*, 17735.

[49] K. Han, Z. Liu, J. Shen, Y. Lin, F. Dai, H. Ye, *Adv. Funct. Mater.* **2015**, *25*, 455.

[50] J. T. Lee, H. Kim, M. Oschatz, D.-C. Lee, F. Wu, H.-T. Lin, B. Zdyrko, W. I. Cho, S. Kaskel, G. Yushin, *Adv. Energy Mater.* **2015**, *5*, 1400981.

[51] J. Ding, H. Zhou, H. Zhang, L. Tong, D. Mitlin, *Adv. Energy Mater.* **2018**, *8*, 1701918.

[52] B. Kalimuthu, K. Nallathamby, *ACS Appl. Mater. Interfaces* **2017**, *9*, 26756.

[53] G. Kresse, J. Hafner, *Phys. Rev. B* **1994**, *49*, 14251.

[54] P. E. Blöchl, *Phys. Rev. B* **1994**, *50*, 17953.

[55] J. P. Perdew, K. Burke, M. Ernzerhof, *Phys. Rev. Lett.* **1996**, *77*, 3865.

[56] S. Grimme, J. Antony, S. Ehrlich, H. Krieg, *J. Chem. Phys.* **2010**, *132*, 154104.